

See discussions, stats, and author profiles for this publication at: <https://www.researchgate.net/publication/253234309>

Eulerian Model for Municipal Solid Waste Gasification in a Fixed-Bed Plasma Gasification Melting Reactor

ARTICLE *in* ENERGY & FUELS · JULY 2011

Impact Factor: 2.79 · DOI: 10.1021/ef200383j

CITATIONS

8

READS

105

4 AUTHORS, INCLUDING:



[Qinglin Zhang](#)

KTH Royal Institute of Technology

10 PUBLICATIONS 112 CITATIONS

SEE PROFILE



[Weihong Yang](#)

KTH Royal Institute of Technology

119 PUBLICATIONS 1,206 CITATIONS

SEE PROFILE



[Włodzimierz Błasiak](#)

KTH Royal Institute of Technology

69 PUBLICATIONS 843 CITATIONS

SEE PROFILE

Eulerian Model for Municipal Solid Waste Gasification in a Fixed-Bed Plasma Gasification Melting Reactor

Qinglin Zhang,^{*,†} Liran Dor,[‡] Weihong Yang,[†] and Wlodzimierz Blasiak[†]

[†]Energy and Furnace Technology Division, Royal Institute of Technology, Brinellvägen 23, S-10044 Stockholm, Sweden

[‡]Environmental Energy Resources, Limited, 7 Jabotinski Street, 52520 Ramat-Gan, Israel

ABSTRACT: Plasma gasification melting (PGM) is a promising waste-to-energy process, which provides many features superior to those of conventional gasification. In this work, a steady Euler–Euler multiphase model is developed to predict the performance of municipal solid waste (MSW) gasification inside a PGM reactor. The model considers the main chemical and physical processes, such as drying, pyrolysis, homogeneous reactions, heterogeneous char reactions, and melting of the inorganic components of MSW. The model is validated by one experimental test of a pilot reactor. The characteristics of PGM gasification, such as temperature distribution, syngas composition, tar yield, and energy conversion ratio (ECR, chemical energy of the gas phase divided by the total energy input), at the proposed condition are discussed. A total of nine cases are used to investigate the effects of the equivalence ratio (ER) and plasma power with a fixed flow rate of MSW. It is found that the ER has a positive effect on the cold gas efficiency of PGM gasification. However, the increase of the ER is restricted by the peak temperature. The influence of the plasma power then is not obvious for PGM gasification.

1. INTRODUCTION

Municipal solid waste (MSW) is one of the major potential energy sources. Among various waste-to-energy processes, gasification is recognized as an important technology.¹ In recent years, various MSW gasification technologies have been developed,^{2–4} while plasma gasification melting (PGM) is one of the promising technologies. In the PGM, gasification is combined with thermal plasma technology. High-temperature plasma torches are applied to provide both heat for melting the inorganic components and sensible heat for gasification. In comparison to conventional gasification, the PGM technology has advantages, such as higher syngas lower heating value (LHV) and higher energy efficiency. Moreover, the PGM technology provides a wise solution for problems related to bottom ash because the inorganic components of MSW are melted and form a vitrified slag.

The characteristics of PGM were studied experimentally in a pilot PGM reactor located in Yblin, Israel.⁵ The results show that the PGM is promising in treating MSW and producing high-quality syngas. However, it was also found that the syngas yield and quality highly depend upon the operation parameters, such as the air feeding rate and power of plasma torches. Considering the high expenses of running the pilot reactor, it is not practical to study the detail influences of different operation parameters only by experiments. Essentially, the PGM reactor is an updraft fixed-bed gasifier. From this point of view, gasification models can be used to predict the performance of PGM, thus helping the designing and optimizing of a PGM reactor. Several numerical models of fixed-bed gasification have been found in the literature.^{6–10} Most of them are one-dimensional models that do not consider the influence of the reactor structure and shape.^{6–9} Rogel and Aguilon¹⁰ developed a one-dimensional (1D) + two-dimensional (2D) model, which solves the conservation equations of the gas phase in a 2D system and solves the conservation equations of

the solid phase in a 1D system. In the authors' opinion, full 2D simulation for fixed-bed gasification was not investigated in detail.

The object of this work is to develop a 2D fixed-bed gasification model for the PGM process. This work is based on a previous model study on fixed-bed gasification with high preheated air.¹¹ In the presented model, the Euler–Euler multiphase method is applied. The main chemical and physical processes, such as drying, pyrolysis, homogeneous reactions, heterogeneous char reactions, and melting of the inorganic components of MSW, are considered in this model. Ansys Fluent 12.1 is used as a tool to do the above work.

Initially, simulation results are examined with measured results. Thereafter, the model is used as a tool to analyze the performance of the system by varying different operation parameters, such as the air feeding rate and plasma power. Attention is focused on the syngas composition, tar yield, and system energy efficiency.

2. PILOT REACTOR

A pilot PGM reactor is located in Yblin, Israel, with a designed capacity of 12–20 tons of MSW per day. The main scheme of the reactor is shown in Figure 1. The reactor is composed of two main parts: the reaction shaft and the melting chambers.

Plasma torches are placed at the ceiling of the melting chamber. Primary air flows into the melting chamber through the torches, where it is ionized, therefore forming plasma jets, which extend beyond the tip of the torches. The temperature of the plasma jets reaches up to 6000 K. The plasma jets supply the

Received: March 11, 2011

Revised: June 29, 2011

Published: July 07, 2011

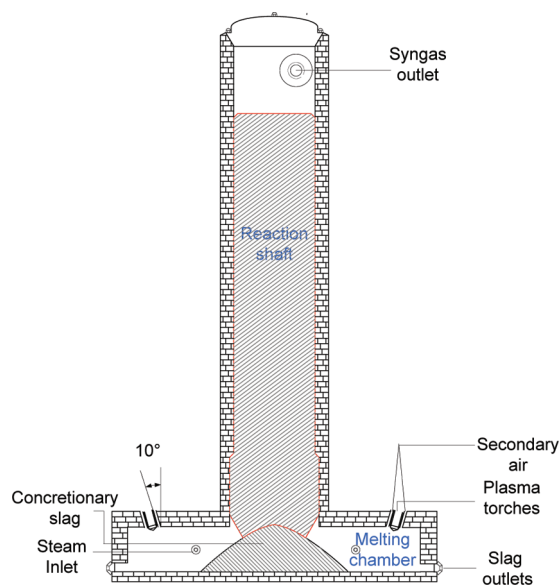


Figure 1. Scheme of the PGM reactor in the demonstration plant.

necessary heat to melt the inorganic components of the MSW in the bottom of the reactor. Secondary air nozzles are placed around plasma torches. Secondary air is injected through secondary air nozzles at room temperature. The flow rate of secondary air is adjustable; thus, the feeding rate of total air can be controlled. An airtight feeding pipe is placed at the top of the reaction shaft. MSW is fed into the reactor intermittently from the shaft top every half an hour. The total height of the reaction shaft is 7.02 m, and the height of the fixed bed is 6.11 m.

To measure the temperature distributions inside the reactor, thermocouples were placed both along the gasifier shaft and in the syngas conduit. A probe was placed in the syngas conduit to obtain syngas samples, which were sent to a gas analyzer for composition analysis. The total syngas yield was then measured by a flowmeter placed in the syngas conduit. Detailed information about the reactor can be found in our previous publication.⁵

3. NUMERICAL MODEL

The Euler–Euler multiphase approach is applied in this work. The conservation equations of mass, momentum, and energy are solved for both gas and solid phases. Mass, momentum, and energy exchanges between phases are allowed. To ensure convergence of the model, the approach is simplified by disregarding the gas–solid stress terms in the momentum equation of the solid phase. The turbulence of the gas phase is simulated with the standard k – ε turbulence model.

A total of 11 gaseous species and 5 solid species are defined in the model. The main chemical and physical processes, such as drying, pyrolysis, homogeneous reactions, heterogeneous char reactions, and melting of the inorganic components of MSW, are considered in this model. For heterogeneous char reactions, the reaction rates are calculated using an unreacted shrinking core model. The reaction rates of homogeneous reactions are determined by considering both the kinetic rates and turbulent mixing rates.

The flow of the slag is ignored. The melting of inorganic components of solid is simulated by setting mass and energy sinks for the solid phase at the melting area, which is determined by experience.

3.1. Governing Equations. **3.1.1. Gas Phase.** The Eulerian conservation equations for species mass, momentum, and energy are solved for the gas phase. The equations are written as follows:¹²

$$\frac{\partial}{\partial t}(\alpha_g \rho_g Y_i) + \nabla(\alpha_g \rho_g Y_i \vec{v}_g) = \dot{m}_i + S_i \quad (1)$$

$$\frac{\partial}{\partial t}(\alpha_g \rho_g \vec{v}_g) + \nabla(\alpha_g \rho_g \vec{v}_g \vec{v}_g) = -\alpha_g \nabla p + \nabla \bar{\tau}_g + \alpha_g \rho_g \vec{g} + K_{sg}(\vec{v}_s - \vec{v}_g) + \dot{m}_{sg} \vec{v}_{sg} \quad (2)$$

$$\frac{\partial}{\partial t}(\alpha_g \rho_g h_g) + \nabla(\alpha_g \rho_g \vec{v}_g h_g) = -\alpha_g \frac{\partial p}{\partial t} + \bar{\tau}_g : \nabla \vec{v}_g - \nabla \bar{q}_g + S_g + Q_{sg} + \dot{m}_{sg} h_{sg} \quad (3)$$

3.1.2. Solid Phase. The solid phase is treated as an interpenetrating continuous phase. The continuity equation for the j th species in the solid phase is similar to that in the gas phase.

$$\frac{\partial}{\partial t}(\alpha_s \rho_s Y_j) + \nabla(\alpha_s \rho_s Y_j \vec{v}_s) = \dot{m}_j + S_j \quad (4)$$

The momentum equation of the solid phase is written as

$$\begin{aligned} \frac{\partial}{\partial t}(\alpha_s \rho_s \vec{v}_s) + \nabla(\alpha_s \rho_s \vec{v}_s \vec{v}_s) \\ = -\nabla p_s + \nabla \bar{\tau}_s + \alpha_s \rho_s \vec{g} - \dot{m}_{sg} \vec{v}_{sg} \end{aligned} \quad (5)$$

where p_s and $\bar{\tau}_s$ denote the solid pressure and shear stress, which are defined to express the normal and shear stress parts of solid-phase stress. The solid-phase stress is a function of the solid volume fraction. At a fixed-bed condition, the value of ∇p_s , which is several orders of magnitude larger than the fluid–solid stress, becomes the main driving force of granular flow.^{13,14} In other words, the influence of the fluid–solid stress on solid motion can be ignored (the detailed numerical expressions of the solid-phase stress and fluid–solid stress are introduced in the next section). This idea was used by Johnson and Jackson¹⁵ to describe nonreaction shearing granular flow. In the present work, the idea is also adopted, so that the fluid–solid stress term is disregarded in the solid-phase momentum equations. This simplification is very helpful for the convergence of the solid momentum equation because it largely prevents the solution of interphase nonlinear terms, which is the main cause of nonconvergence for the Euler–Euler approach.

The energy equation of the solid phase is written as

$$\begin{aligned} \frac{\partial}{\partial t}(\alpha_s \rho_s h_s) + \nabla(\alpha_s \rho_s \vec{v}_s h_s) = -\alpha_s \frac{\partial p}{\partial t} + \bar{\tau}_s : \nabla \vec{v}_s - \nabla \bar{q}_s \\ + S_s + Q_{gs} - \dot{m}_{sg} h_{sg} \end{aligned} \quad (6)$$

3.1.3. Gas–Solid Stress. The gas–solid stress is ignored for the solid phase. However, it is considered in the momentum equation of the gas phase. The gas–solid stress is simulated using the Ergun equation.¹⁶ The interphase momentum exchange coefficient K_{sg} is written as

$$K_{sg} = 150 \frac{\alpha_s(1 - \alpha_g)\mu_g}{\alpha_g d_s^2} + 1.756 \frac{\rho_g \alpha_s |\vec{v}_s - \vec{v}_g|}{d_s} \quad (7)$$

3.1.4. Solid-Phase Stress. The solid phase stress is composed of two parts: the normal stress part and the shear stress part. For fixed-bed gasification, the flow of the solid phase should be treated as a plastic flow.¹⁷ The normal stress part is expressed by solid pressure p_s .¹⁸

$$p_s = \alpha_s p^* \quad (8)$$

Table 1. Kinetics Data for Primary and Secondary Pyrolysis

reaction	reaction rate	reference
primary pyrolysis of the cellulosic group	$r = 3.20 \times 10^5 (1 - \alpha_g) \exp\left(\frac{-1.60 \times 10^4}{T_s}\right) \rho_{v1}$	32
primary pyrolysis of the plastic group	$r = (1 - \alpha_g) \sum_{i=1}^6 \left(Y_i A_{3,i} \exp\left(\frac{-E_{3,i}}{RT_s}\right) \right) \rho_{v2}$	33
secondary pyrolysis	$r = 9.55 \times 10^4 \alpha_g \exp\left(\frac{-1.12 \times 10^4}{T_g}\right) \rho_{tar1}$	29

p^* is expressed by an empirical power law

$$p^* = A(\alpha_g - \alpha_g^*)^n \quad (9)$$

where α_g^* is the gas volume fraction at minimum fluidization. Empirical values of $A = 10^{25}$ Pa and $n = 10$ are used.

For the shear stress part, only the frictional viscosity is considered. Because the flow of the solid phase is dense flow, where the solid volume fraction for the solid phase is near the packing limit, Schaeffer's formulation¹⁹ of frictional viscosity is applied.

$$\mu_s = \frac{p_s \sin \phi}{2\sqrt{I_{2D}}} \quad (10)$$

3.1.5. Interphase Heat Transfer. The intensity of heat exchange between the solid and gas phases is assumed to be a function of the temperature difference between the solid and gas phases.

$$Q_{sg} = -Q_{gs} = k_{sg}(T_s - T_g) \quad (11)$$

The heat-transfer coefficient is written as

$$k_{sg} = \frac{6\kappa_g \alpha_g Nu_s}{d_s^2} \quad (12)$$

Here, Nu_s is the Nusselt number correlated by Gunn.²⁰

$$Nu_s = (7 - 10\alpha_g + 5\alpha_g^2)(1 + 0.7Re_s^{0.2}Pr_g^{0.33}) + (1.33 - 2.4\alpha_g + 1.2\alpha_g^2)Re_s^{0.7}Pr_g^{0.33} \quad (13)$$

3.2. Reaction Rates. **3.2.1. Drying.** Drying is the first process to take place for feedstock during gasification. Despite its seemingly simplicity, drying of feedstock is a complex combination of three steps: evaporation of free water, desorption and evaporation of absorbed water, and separation of chemically bound water.²¹ In our work, a drying model that is popularly used in fixed-bed combustion or gasification of MSW and biomass^{22–26} is applied

$$r_1 = A_v k_m (C_{moi} - C_{H_2O}) \quad \text{when } T_s < 100^\circ\text{C} \quad (14)$$

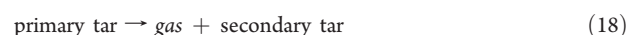
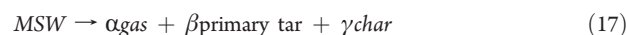
or

$$r_1 = Q_{sg}/H_{evp} \quad \text{when } T_s \geq 100^\circ\text{C} \quad (15)$$

The mass-transfer coefficient k_m is calculated according to the Sherwood number.^{27,28}

$$k_m = \frac{ShD}{d} \quad (16)$$

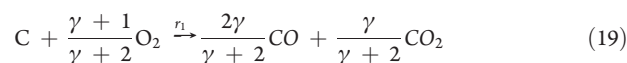
3.2.2. Pyrolysis. Pyrolysis is the thermal decomposition of solid fuels in the absence of oxidizers. Because of the complexity in both reaction paths and products generated, the detail kinetics of pyrolysis is still unclear. Therefore, overall kinetics expressions are commonly used in pyrolysis models. In this work, a two-step pyrolysis model is applied. The pyrolysis of MSW is divided into two steps. At first, MSW decomposes into char, gas, and primary tar. Then, the primary tar decomposes into gas and secondary tar by thermal cracking.⁹



It has been confirmed by experiments that the two-step pyrolysis model can correctly predict the pyrolysis yields, especially tar yields at various conditions.^{29,30} It is very appropriate for modeling pyrolysis in the updraft fixed-bed gasification because the tar problem is the most significant in this constitution.

MSW is the mixture of different species. Generally, most of the organic components of MSW can be divided into two groups: the cellulosic group (wood, paper, cardboard, textile, etc.) and the plastic group (polystyrene, polypropylene, polyethylene, polyvinyl chloride,³¹ etc.). The pyrolysis characters of these two groups are different. In this work, the differences are considered using individual pyrolysis kinetics for each group (shown in Table 1). The interactions between species are not considered in this model.

3.2.3. Heterogeneous Char Reactions. Heterogeneous char reactions involved in this model include the following overall reactions:



For reaction 20, the ratio of produced CO/CO₂ γ is calculated as³⁴

$$\gamma = CO/CO_2 = 2500 \exp(-6420/T_g) \quad (22)$$

The heterogeneous reaction rates are estimated using the unreacted shrinking core model, in which the real reaction rate depends upon surface film diffusion and reaction kinetics.³⁵

$$r_i = \left(\frac{1}{v_{i,j} M_j} \right) \frac{A_v \rho_j}{\frac{1}{k_m} + \frac{1}{k_{ri}}} \quad i = 1 - 3, j = O_2, H_2O, CO_2 \quad (23)$$

Table 2. Pre-exponent Factors and Activation Energy of Heterogeneous and Homogeneous Reactions

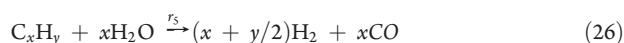
value of i	A_i	E_i (J mol ⁻¹)	reference
1	87.1 m s ⁻¹ K ⁻¹	1.13 × 10 ⁵	36
2	5.71 m s ⁻¹ K ⁻¹	1.30 × 10 ⁵	37
3	589 m s ⁻¹ K ⁻¹	2.23 × 10 ⁵	35
4	0.03 m ³ kmol ⁻¹ s ⁻¹	6.03 × 10 ⁴	38
5	3.0 × 10 ⁸ m ³ kmol ⁻¹ s ⁻¹ K ⁻¹	1.254 × 10 ⁵	40

For all heterogeneous char reactions, a first order of reaction is assumed with respect to gaseous reactants. The kinetic rate is calculated as

$$k_{ri} = A_i T_s \exp\left(\frac{-E_i}{RT_s}\right) \quad (24)$$

The values of pre-exponent factors and activation energy of heterogeneous reactions are shown in Table 2.

3.2.4. Homogeneous Gas-Phase Reactions. Because of the low ER value in a typical PGM process, most of the oxygen will be consumed in the char oxidation section; therefore, combustion of combustible gases can be ignored. The water–gas shift reaction, as well as cracking and reforming of light hydrocarbons (LHCs) is considered in this work.



Chemical reaction rates are considered by choosing the minimum of the kinetic rates and turbulent mixing rates.

$$r_i = \min(r_{ti}, r_{ti}), \quad i = 4-5 \quad (27)$$

Turbulent mixing rates are calculated using the eddy dissipation model

$$r_{ti} = 4.0\rho \frac{\varepsilon}{k} \min\left(\frac{Y_j}{v_{i,j}M_j}\right) \quad (28)$$

where j denotes any reactant of reaction i .

The water–gas shift reaction is considered as a reversible reaction. The kinetics of the water–gas shift reaction is taken from the work by Grebenshchikova.³⁸

$$r_{r4} = \alpha_g A_4 \exp\left(\frac{-E_4}{RT_g}\right) \frac{C_{\text{CO}} C_{\text{H}_2\text{O}}}{M_{\text{CO}} M_{\text{H}_2\text{O}}} - \frac{\alpha_g A_4 \exp\left(\frac{-E_4}{RT_g}\right)}{K_c} \frac{C_{\text{CO}_2} C_{\text{H}_2}}{M_{\text{CO}_2} M_{\text{H}_2}} \quad (29)$$

where K_c is the equilibrium constant. The value of K_c is given by Bensen.³⁹

$$K_c = \exp\left[\frac{1}{RT_g} \left(11321 - 31.08T_g + 3T_g \ln T_g - 2.8 \times 10^{-4} T_g^2 - \frac{91500}{T_g}\right)\right] \quad (30)$$

The kinetics of the steam-reforming reaction is taken from Jones et al.⁴⁰

$$r_{r5} = \alpha_g A_5 T_g \exp\left(\frac{-E_5}{RT_g}\right) C_{\text{CH}_4} C_{\text{H}_2\text{O}} \quad (31)$$

3.3. Geometry and Boundary Conditions. Geometry used in this work should be a reflection of the real three-dimensional (3D) geometry, so that it can capture most flow characteristics of a real PGM process. The geometry of the trial gasifier is approximately symmetrical

Table 3. Boundary Conditions of Simulated Cases with Dimensionless Numbers

case number	plasma power (kW)	plasma air (kg/h)	secondary air (kg/h)	ER	DPER
1	240	120	10	0.043	0.118
2	240	120	40	0.053	0.118
3 (base case)	240	120	60	0.060	0.118
4	240	120	80	0.067	0.118
5	240	120	110	0.077	0.118
6	200	100	80	0.060	0.098
7	220	110	70	0.060	0.108
8	260	130	50	0.060	0.128
9	280	140	40	0.060	0.138

in the width direction; therefore, the longitudinal section of the gasifier can be used as the 2D geometry. Because the void fraction of the hillock of concretionary slag is very small, the hillock was excluded from the flow field. The total number of mesh cells is 10 107. In the areas associated with plasma injections and secondary air injections, the mesh was refined.

To express the feeding of MSW, a mass source of the solid phase was defined at the top of the fixed bed. Because this is a steady model, the feeding of MSW is assumed to be continuous. For all cases, the feeding rate is 600 kg/h. Mass flow inlet conditions are defined at the corresponding positions of plasma air and secondary air inlets. The outlet of syngas is defined as a pressure outlet. The relative pressure at the outlet is set to −700 Pa, which is the measured result for the pilot reactor. The melting of unreacted solid residual is represented by a mass and energy sink of the solid phase. Another energy sink is defined in the melting chambers to express the heat transfer from the gas phase to slag. The motion of slag after melting is ignored in this model. The reactor walls are defined as no-slip walls. An empirical temperature distribution is defined at the reactor wall to calculate the heat loss from the wall.

Altogether nine cases with different plasma powers and air feeding rates are simulated with this model. To increase the versatility of the results, dimensionless numbers are used to characterize and classify the operation parameters of the PGM process.

The amount of available air per kilogram of MSW is represented by the equivalence ratio (ER), defined as

$$ER = \frac{(\dot{M}_{\text{air}}/\dot{M}_{\text{MSW}})}{(\dot{M}_{\text{air}}/\dot{M}_{\text{MSW}})_{\text{stoic}}} \quad (32)$$

where $\dot{M}_{\text{air}}/\dot{M}_{\text{MSW}}$ is the air/MSW mass flow ratio in the real cases and $(\dot{M}_{\text{air}}/\dot{M}_{\text{MSW}})_{\text{stoic}}$ is the air/MSW mass flow ratio for a stoichiometric combustion where the fuel is fully combusted.

The amount of plasma energy per kilogram of MSW is expressed by the dimensionless plasma energy ratio (DPER), which is defined as

$$DPER = \frac{P_{\text{pla}}}{LHV_{\text{MSW}} \dot{M}_{\text{MSW}}} \quad (33)$$

where P_{pla} is the heat power of plasma generators, LHV_{MSW} is the low heating value of raw MSW, and \dot{M}_{MSW} is the mass flow rate of raw MSW.

Despite the common boundary conditions, the detailed boundary conditions for all cases are expressed by the above dimensionless numbers, as found in Table 3. The base case is a standard case, in which the operation parameters are set to a “reasonable” value. The choice of the operation parameters for the base case is based on experiences from a series of trial runs. To study the influence of ER and DPER, all cases are divided into two groups. The first group includes cases 1–5, which aims

Table 4. MSW Proximate and Ultimate Analyses

Proximate Analysis (on a Dry Basis, except Moisture)	
moisture (%)	20.0
fixed carbon (%)	10.7
volatile (%)	77.6
ash (%)	11.7
Ultimate Analysis (on a Dry Basis)	
carbon (%)	50.5
hydrogen (%)	5.6
oxygen (%)	30.7
nitrogen (%)	1.1
chlorine (%)	<0.1
sulfur (%)	0.3
LHV of raw MSW (MJ/kg)	12.89

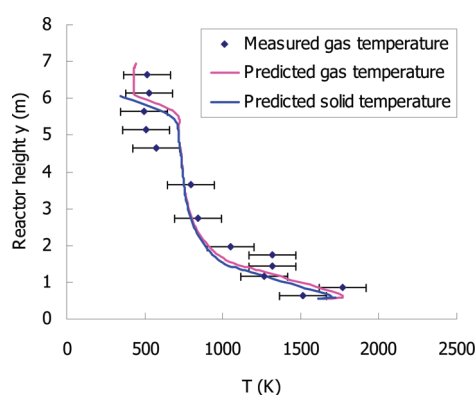


Figure 2. Temperature distribution along the shaft height of the base case.

at studying the influence of ER. The second group (including cases 6–9, as well as the base case) is used to study the influence of DPER.

3.4. MSW Properties. Feedstock used by the trial runs is MSW collected in Israel. Proximate and ultimate analyses have been made on a sample of this MSW. The results are shown in Table 4.

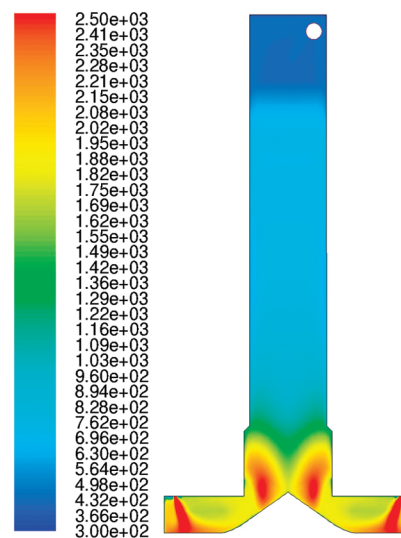
4. RESULTS AND ANALYSIS

4.1. Analysis of the Base Case. *4.1.1. Comparison of Predicted and Measured Results.* To evaluate the availability of the model, simulation data of the temperature distribution along the reaction shaft axis as well as the syngas composition were compared to measure data obtained from test runs of the base case. Results are shown in Figure 2 and Table 5. The predicted and measured temperature profiles fit each other well. However, a slight deviation was found at the reactor height of 4.5–6.1 m. Two reasons can explain this deviation. First, the assumption of continuous feeding of MSW in the model leads to imprecise temperature prediction near the fixed-bed top. Second, the uncertainty of pyrolysis mechanisms also affects the accuracy of the temperature prediction in the pyrolysis section. Considering the possible variation of MSW composition with time and area, the disparities between predicted and measured results are acceptable.

Table 5 shows a comparison of predicted and measured syngas yields and composition for the base case. It can be seen that the predicted yields and compositions of syngas are also in good

Table 5. Syngas Yield and Compositions for the Base Case

syngas	predicted	measured	deviation
H ₂ (vol %, wet basis)	19.19	19.50	−0.016
CO (vol %, wet basis)	17.21	15.20	0.132
LHCs (vol %, wet basis)	7.22	6.90	0.046
incombustible gases (vol %, wet basis)	56.68	58.40	−0.029
syngas yield [N m ³ (kg of MSW) ^{−1} , wet basis]	1.062	1.063	−0.001



Contours of Static Temperature (phase-1) (K)

Figure 3. Gas temperature distribution (K) in the base case.

agreement with the measurements, despite an acceptable deviation related to CO. The model slightly overestimates the CO volume fraction, with the deviation equal to 0.132. It is believed that this deviation is mainly caused by the overestimation of the peak temperature because of the disregarding partial melting in the fixed bed. Generally, the deviations of the predicted results are in an acceptable level for understanding the characteristics of the PMG process.

4.1.2. Temperature Profiles. The distribution of the gas temperature in the base case is shown in Figure 3. It is found that the plasma air temperature reduces rapidly because of radiation and heat exchange with unmelted inorganics. During this process, the plasma air also mixes with secondary air. The average gas temperature at the gas–bed boundary is about 1800 K. When air flows into the fixed bed, the gas temperature increases dramatically to around 2400 K because of char combustion. Then, the gas temperature rapidly decreases to around 1000 K. This decrement can be explained by intense heat exchange between phases and endothermic char gasification. Because the gasification agent used in this case is air, the main char gasification here should be the Boudouard reaction. When the gas temperature reaches 1000 K, the temperature decreasing rate starts to slow gradually. In this zone, the Boudouard reaction generally stops. The heat transfer between the gas and solid phases also becomes slow because of the decrease of temperature differences (see Figure 2). At the reactor height of 5.0–6.1 m,

where pyrolysis and drying of MSW take place, the gas temperature starts to decrease visibly again from around 860 to 450 K. After gas flows out of the fixed-bed area, no reaction or heat exchange happens for gases, so that the gas temperature nearly keeps constant.

4.1.3. Non-uniformity of Temperature Distributions in Horizontal Sections. In the PGM reactor, the temperature distribution in a horizontal section is not uniform. This non-uniformity can be reflected from Figure 3. Figure 4 shows detailed gas temperature distributions at different horizontal sections in the base case. The non-uniformity of the gas temperature is most significant at the $y = 1.0$ m section, where the gas temperature varies from 1430 to 2080 K. The peak temperature in this section

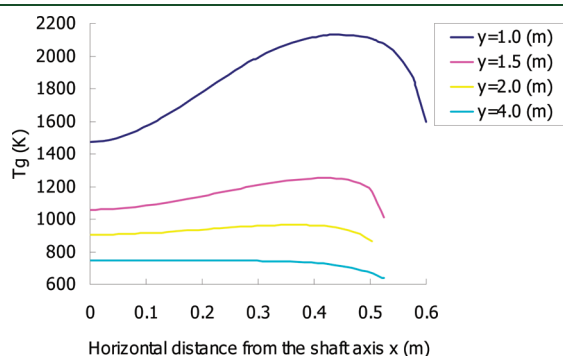


Figure 4. Gas temperature distributions in different horizontal sections in the base case.

appears at the $0.40 < x < 0.55$ m area, which is corresponding to the horizontal position of gas–bed interface at the $y = 1.0$ m section. The position of the peak temperature denotes that char combustion only occurs in a thin layer near the gas–bed interface. From an engineering point of view, a high peak temperature should be prevented because it causes problems, such as bridging and damage of the reactor wall. To prevent the problems caused by a high peak temperature, the intensity of char combustion has to be restricted by controlling the ER value. The influence of the ER on PGM gasification will be discussed later.

The temperature distribution in the $y = 2.0$ m section shows a similar trend to the $y = 1.0$ m section. However, the difference between the shaft axis temperature and peak temperature dramatically decreases to about 150 K. It denotes that the non-uniformity of the gas temperature becomes weak with an increasing height because of horizontal heat transfer. In the $y = 3.0$ m and $y = 4.0$ m sections, the differences between the axis temperature and peak temperature are not visible. In all of these four sections, the temperature decline near the reactor wall is caused by heat loss from the reactor wall.

4.1.4. Composition Profiles. Parts a–e of Figure 5 show the volume fractions of CO, H₂, LHCs, CO₂, and H₂O in the gas phase. Because only air is used as a gasification agent in this work, the water–gas reaction and water–gas shift reaction are restrained. H₂ can only be produced from the pyrolysis step. This phenomenon is well-presented in Figure 5a. A similar trend is also found for LHCs. CO is generated from both char combustion and pyrolysis. As in Figure 5c, the volume fraction of CO reaches about 18% after heterogeneous char reactions.

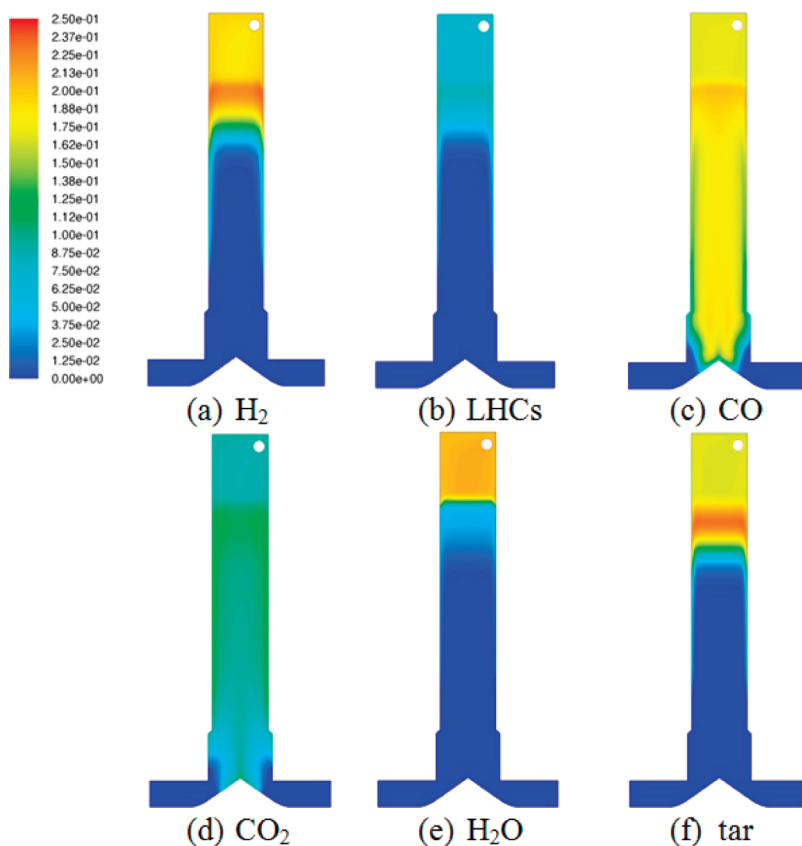


Figure 5. Syngas compositions of the base case: (a) molar fraction of CO, (b) molar fraction of H₂, (c) molar fraction of LHCs, (d) molar fraction of CO₂, (e) molar fraction of H₂O, and (f) mass fraction of tar.

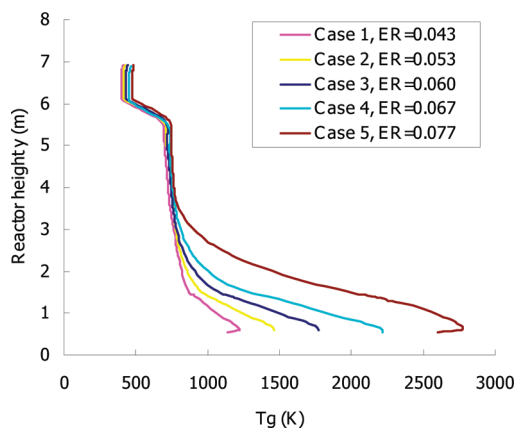


Figure 6. Temperature distribution along the shaft height for different ER values.

The volume fraction of CO does not change much during pyrolysis. However, the yield of CO from pyrolysis is still remarkable because the gas volume increases significantly during pyrolysis.

A significant aspect of the PGM technology is that it produces a high-quality syngas. As we can see in Figure 5, the volume fractions of CO and H₂ reach around 20% at the syngas outlet and the volume fraction of LHCs is about 7%. The LHV of the wet syngas reaches about 6.79 MJ N⁻¹ m⁻³ in the base case, which is a very high value for MSW gasification. It is believed that the high LHV value is mainly due to a low ER value in the PGM process, which prevents the direct dilution of combustible gases from N₂. A low ER also provides a sub-stoichiometric O₂ environment, which suppresses the formation of CO₂.

The tar yield is one of the main problems involved in the fixed-bed gasification, which reduces the energy efficiency and causes blockage to the pipeline of syngas. The mass fraction of tar in the gas phase is demonstrated in Figure 5f. The tar mass fraction at the syngas outlet is about 16.8%, which reflects a tar yield ratio of 0.193 kg/kg of MSW.

4.2. Influence of ER. The ER is one of the most important operation parameters of gasification. It determines the level of MSW partial combustion and directly influences the temperature profile, syngas composition, and stability of the gasification process. The ER required for a typical PGM air gasification varies from 0.05 to 0.10, while the ER for conventional gasification is about 0.3. Few scientific works have been found on the characteristics of gasification in low ER conditions. Studying the influence of ER on the performance of a PGM gasifier is of both scientific and engineering value.

In this study, five cases with different ER values are simulated. From cases 1–6, the ER value varies from 0.043 to 0.077. The DPFR value for all cases is set as 0.118.

4.2.1. Gas Temperature Distribution. Figure 6 shows the predicted gas temperature distributions at the shaft axis with different ER values. From cases 1–5, the gas temperature shows an increasing trend with ER. This phenomenon is more significant in the lower part of the reaction shaft, where the temperature increases from 1250 to 2750 K. The temperature increase with ER is explained by prompted char combustion because of increases of the O₂ flow rate. According to chemical equilibrium calculation, for 100% conversion of carbon in char, the ER value should be about 0.13, which is much higher than the ER values in the simulated cases. No doubt that the increasing

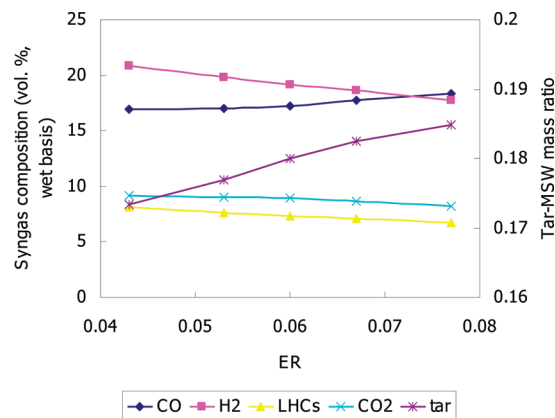


Figure 7. Predicted temperature distributions for different DPFR values.

trend of the gas temperature will continue if the ER keeps increasing. However, to restrict the peak temperature under 2273 K, the ER value in PGM air gasification should be controlled less than 0.067. This may result in insufficient combustion of char, which leads to low energy efficiency.

4.2.2. Syngas Composition. Figure 7 shows the variation of syngas composition, as well as the tar/MSW mass ratio, with the ER value. It is found that, when the ER increases, the volume fractions of H₂, LHCs, and CO₂ decrease and the volume fraction of CO increases. The increasing CO volume fraction can be explained by prompted char combustion with an increasing ER, while the decreasing H₂ and LHC volume fractions are explained by dilution of syngas by introduced N₂. It is interesting to find that the CO₂ volume fraction also decreases when ER increases. This phenomenon may be caused by an increasing combustion temperature with ER, which prevents the formation of CO₂ during char combustion. Moreover, the tar/MSW mass ratio is also increasing slightly with ER. This increase is the result of an increasing heating rate with ER in the pyrolysis zone.

4.2.3. Energy Conversion Ratio (ECR). To quantify the energy conversion from MSW to syngas, the ECR was defined and used.

$$ECR = \frac{\dot{M}_{H_2} LHV_{H_2} + \dot{M}_{CO} LHV_{CO} + \dot{M}_{LHC} LHV_{LHC}}{\dot{M}_{MSW} LHV_{MSW} + P_{pla}} \times 100\% \quad (34)$$

The ECR is a very important process parameter that characterizes the combustion value of the gas phase. It illustrates the variation of syngas composition during the gasification process and can be used as an index for the gas quality. The ECR value at the syngas outlet is named cold gas efficiency (CGE),⁴⁰ which is widely used as a standard criteria for the energy efficiency of gasification. In the PGM process, the original definition of CGE was modified slightly.⁵

Figure 8 shows the ECR value in the horizontal sections along the shaft height for cases 1–5. In all cases, the energy conversions mainly happen in two sections: char combustion and pyrolysis. It is found that the ER has a positive effect on energy conversion in the char combustion section. When ER varies from 0.043 to 0.077, the ECR will increase from 0.02 to about 0.06. No doubt that this increasing is caused by prompted char combustion because of increasing O₂. The increase of the gas temperature with ER also has a positive effect on energy conversion because it pushes reaction 20 to produce more CO rather than CO₂.

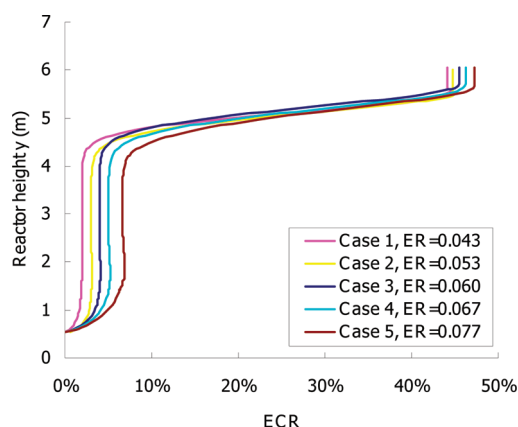


Figure 8. ECR values along the shaft height for different ER values.

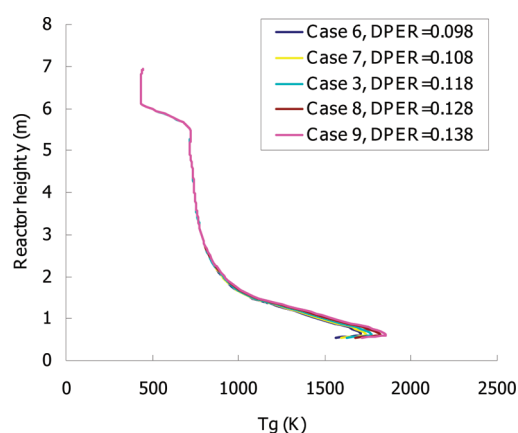


Figure 9. Temperature distributions along the shaft height for different DPER values.

Volatiles take up to 77.6% of the total MSW mass. Most of the energy conversion happens in the pyrolysis section, which is corresponding to the shaft height of 4.5–5.5 m in the reactor. Only a slight negative effect on energy conversion is found for ER. The proper reason is that the enhanced heating rate is caused by an increasing ER, which results in an increasing tar yield. The increase of the tar yield has been demonstrated in Figure 7.

Because the influence of ER on ECR is more significant in the char combustion section, it is possible to increase the system CGE by increasing ER. However, as discussed previously, the increase of ER is restricted by the peak temperature. The ER value in PGM air gasification should be lower than 0.067. A practical solution to this problem is to inject additional steam into the reactor. The numerical study on air and steam gasification in a PGM reactor will be presented in the future.

4.3. Influence of DPER. The most important significance of the PGM process is the high-temperature plasma air injected from the bottom of the reactor. The high-temperature plasma flow supplies heat for both gasification residual melting and reactions related to the gasification process. The value of DPER may directly influence the temperature profile, syngas composition, tar yield, and stability of the gasification process. In this work, the influence of DPER is investigated. Together with the base case, five cases with different DPER values are simulated (cases 3 and 6–9). The value of DPER varies from 0.098 to 0.138. The ER value for all cases is set as 0.060.

Figure 9 shows the predicted gas temperature distributions at the shaft axis with different DPER values. It was very interesting to find that the temperature distributions for all of these cases are similar. When DPER increases from 0.098 to 0.138, the increment of the peak temperature along the shaft axis is less than 200 K. A possible explanation for this phenomenon is the heat loss in the melting chambers. First, an intense heat transfer exists between plasma air and slag because the high-temperature and high-velocity plasma flow was directly injected into the slag pool, which exists at the bottom of the melting chamber. Second, the strong heat radiation leads to large heat loss from the chamber wall. During the running of the pilot reactor, it is found that heat loss from the chamber wall reaches about 30% of the total plasma power. It is also found that the heat loss increases with the DPER value.

A thermodynamic calculation is performed by authors to estimate the lower limit of DPER to satisfy the heat request for melting the inorganic components. The result shows that, when the DPER value is larger than 0.09, the plasma flow can supply enough heat for the melting process. From the viewpoint of energy efficiency, the optimal DPER value for PGM air gasification should be about 0.09.

5. CONCLUSION

(1) The PGM system was examined for air gasification by a 2D Euler–Euler multiphase model. The model considered all major chemical and physical processes involved during PGM gasification. The model showed significant agreement with the measurement from the base case. (2) Analysis of the base case by means of computational fluid dynamics (CFD) revealed that the horizontal temperature distribution inside the reactor was non-uniform. In addition, a maximum peak temperature of the reactor was observed at the gas–solid interface. PGM air gasification provided a higher calorific value of the syngas ($\text{LHV} = 6.79 \text{ MJ N}^{-1} \text{ m}^{-3}$). The tar yield is around 0.193 kg/kg of MSW. (3) A further investigation of the PGM process by means of the developed model revealed that ER has a positive influence on the calorific value of the syngas. An increase of ER from 0.043 to 0.077 showed around a 5% increase in CGE. However, the maximum allowable ER for the present gasification system was restricted to about 0.067 because of the increase in the peak temperature of the reactor. (4) The influence of DPER on PGM air gasification is not obvious. The optimal DPER value was considered as about 0.09, considering energy efficiency. (5) Although PGM air gasification provided a higher calorific value of the syngas ($\text{LHV} = 6.79 \text{ MJ N}^{-1} \text{ m}^{-3}$), a detrimental effect on char conversion was observed. Minimization of this problem will be addressed in our future research.

AUTHOR INFORMATION

Corresponding Author

*Telephone: 0046-8790-8405. Fax: 0046-8207-681. E-mail: qinglin@kth.se.

NOMENCLATURE

A_i = pre-exponential factor of reaction i
 A_v = specific surface area (m^{-1})
 C = mass concentration (kg m^{-3})
 d = particle diameter (m)
 D = diffusion coefficient of vapor in the bulk ($\text{m}^2 \text{s}^{-1}$)
 E_i = activation energy of reaction i
 \vec{g} = gravitational acceleration (m s^{-2})

h = specific enthalpy (J kg^{-1})
 H_{eva} = evaporation heat of the solid material (J kg^{-1})
 k = heat-transfer coefficient ($\text{W m}^{-2} \text{K}^{-1}$)
 k_m = mass-transfer coefficient (m s^{-1})
 k_{ri} = kinetics rate of heterogeneous reaction i (m s^{-1})
 K = interphase momentum exchange coefficient ($\text{kg m}^{-3} \text{s}^{-1}$)
 \dot{m} = mass-transfer rate ($\text{kg m}^{-3} \text{s}^{-1}$)
 M = molar weight (kg kmol^{-1})
 \dot{M} = mass flow rate (kg s^{-1})
 p = pressure (Pa)
 P = power (W)
 q = heat flux (W m^{-2})
 Q = intensity of heat exchange (W m^{-3})
 r = reaction rate ($\text{kmol m}^{-3} \text{s}^{-1}$)
 r_{ri} = kinetic rate of homogeneous reaction i ($\text{kmol m}^{-3} \text{s}^{-1}$)
 r_{ti} = turbulent mixing rate of reactants involved in homogeneous reaction i ($\text{mol m}^{-3} \text{s}^{-1}$)
 R = universal gas constant ($\text{J mol}^{-1} \text{K}^{-1}$)
 S = source term
 Sh = Sherwood number
 t = time (s)
 T = temperature (K)
 \vec{v} = velocity (m s^{-1})
 ν_{ij} = stoichiometric coefficient of reactant j in reaction i
 Y_i = mass fraction of the i th species

Greek Symbols

α = volume fraction
 ρ = density (kg m^{-3})
 $\bar{\tau}$ = stress tensor (Pa)
 μ = dynamic viscosity (Pa s)
 ϕ = angle of internal friction
 κ = thermal conductivity ($\text{W m}^{-1} \text{K}^{-1}$)
 ϵ = turbulent dissipation rate ($\text{m}^2 \text{s}^{-3}$)

Subscripts

air = air
 c = fixed carbon
 CO = carbon monoxide
 CO₂ = carbon dioxide
 C_xH_y = light hydrocarbons
 g = gas phase
 H₂ = hydrogen
 H₂O = steam
 moi = moisture
 MSW = municipal solid waste
 O₂ = oxygen
 pla = plasma
 s = solid phase
 tar1 = primary tar
 v1 = volatile from cellulosic species
 v2 = volatile from plastic species

REFERENCES

- (1) Malkow, T. *Waste Manage.* **2004**, 24 (1), 53–79.
- (2) Filippis, P. D.; Borgianni, C.; Paolucci, M.; Pochetti, F. *Waste Manage.* **2004**, 24 (6), 633–639.
- (3) Choy, K. K. H.; Porter, J. F.; Hui, C. W.; McKay, G. *Chem. Eng. J.* **2004**, 105 (1–2), 31–41.
- (4) Thamavithya, M.; Dutta, A. *Fuel Process. Technol.* **2008**, 89 (10), 949–957.
- (5) Zhang, Q.; Dor, L.; Fenigshtein, D.; Yang, W.; Blasiak, W. *Appl. Energy* **2011** 10.1016/j.apenergy.2011.01.041.
- (6) Syamlal, M.; Bissett, L. *METC Gasifier Advanced Simulation (MGAS) Model*; Morgantown Energy Technology Center: Morgantown, WV, 1992.
- (7) Bryden, K. M.; Ragland, K. W. *Energy Fuels* **1996**, 10, 269–275.
- (8) Hla, S. S. A theoretical and experimental study on a stratified downdraft biomass gasifier. Ph.D. Thesis, The University of Melbourne, Melbourne, Victoria, Australia, 2004.
- (9) Blasi, C. D. *AIChE J.* **2004**, 50 (9), 2306–2319.
- (10) Rogel, A.; Aguilon, J. *Am. J. Appl. Sci.* **2006**, 3 (10), 2068–2075.
- (11) Yang, W.; Ponzio, A.; Lucas, C.; Blasiak, W. *Fuel Proc. Technol.* **2006**, 87 (3), 235–245.
- (12) ANSYS, Inc. *ANSYS FLUENT 12.0 Theory Guide*; ANSYS, Inc.: Canonsburg, PA, 2009.
- (13) Kuipers, J. A. M.; Duin, K. J. V.; Beckum, F. P. H.; Swaaij, W. P. M. *Chem. Eng. Sci.* **1992**, 47 (8), 1913–1924.
- (14) Gldaspow, D.; Ettehadleh, B. *Ind. Eng. Chem. Fundam.* **1983**, 22 (2), 193–201.
- (15) Johnson, P. C.; Jackson, R. *J. Fluid Mech.* **1987**, 176, 67–93.
- (16) Ergun, S. *Chem. Eng. Prog.* **1952**, 48 (2), 89–94.
- (17) Cowin, S. C. *Powder Technol.* **1974**, 9 (2–3), 61–69.
- (18) Syamlal, M.; Rogers, W.; O'Brien, T. J. *MFIX Documentation: Theory Guide*; National Technical Information Service: Springfield, VA, 1993; Vol. 1.
- (19) Schaeffer, S.; Balakrishnan, L. *ICASE Report 90-18: Application of a Reynolds–Stress Turbulence Model to the Compressible Shear Layer*; National Aeronautics and Space Administration (NASA): Washington, D.C., 1990.
- (20) Gunn, D. J. *Int. J. Heat Mass Transfer* **1978**, 21, 467–476.
- (21) Peters, B. *Thermal Conversion of Solid Fuels (Developments in Heat Transfer)*; WIT Press: Billerica, MA, 2002; Vol. 15.
- (22) Yang, Y. B.; Goh, Y. R.; Zakaria, R.; Nasserzadeh, V.; Swithenbank, J. *Waste Manage.* **2002**, 22 (4), 369–380.
- (23) Yang, Y. B.; Nasserzadeh, V.; Goodfellow, J.; Goh, Y. R.; Swithenbank, J. *J. Inst. Energy* **2002**, 75 (S04), 66–80.
- (24) Yang, Y. B.; Yamauchi, H.; Nasserzadeh, V.; Swithenbank, J. *Fuel* **2003**, 82 (18), 2205–2221.
- (25) Yang, Y. B.; Sharifi, V. N.; Swithenbank, J. *Fuel* **2004**, 83 (11–12), 1553–1562.
- (26) Yang, W.; Ponzio, A.; Lucas, C.; Blasiak, W. *Fuel Process. Technol.* **2006**, 87 (3), 235–245.
- (27) Ranz, W. E.; Marshall, W. R. *Chem. Eng. Prog.* **1952**, 48 (3), 141–146.
- (28) Ranz, W. E.; Marshall, W. R. *Chem. Eng. Prog.* **1952**, 48 (4), 173–180.
- (29) Broson, M. L.; Howard, J. B.; Longwell, J. P.; Peter, W. A. *AIChE J.* **1989**, 35 (1), 120–128.
- (30) Liden, A. G.; Berruti, F.; Scott, D. S. *Chem. Eng. Commun.* **1988**, 65 (1), 207–221.
- (31) Sorum, L.; Gronli, M. G.; Hustad, J. E. *Fuel* **2001**, 80 (9), 1217–1227.
- (32) Chan, W. R.; Kelbon, M.; Krieger, B. B. *Fuel* **1985**, 64 (11), 1505–1513.
- (33) Wu, C.; Chang, C.; Hor, J. *Waste Manage.* **1993**, 13 (3), 221–235.
- (34) Arthur, J. A. *Trans. Faraday Soc.* **1951**, 47, 164–178.
- (35) Hobbs, M. L.; Radulovic, F. T.; Smoot, L. D. *Prog. Energy Combust. Sci.* **1993**, 19 (6), 505–586.
- (36) Desai, P. R.; Wen, C. Y. *Computer Modeling of Morgantown Energy Research Center's Fixed Bed Gasifier*; Department of Chemical Engineering, West Virginia University: Morgantown, WV, 1978.
- (37) Yoon, H. W.; Denn, M. M. *AIChE J.* **1978**, 24 (5), 885–903.
- (38) Grebenshchikova, G. B. *Podzemn. Gazif. Uglei* **1957**, 2, 54–57.
- (39) Lowry, H. H. *Chemistry of Coal Utilization*; John Wiley and Sons, Inc.: New York, 1981; Supplementary Vol. 2.
- (40) Reimert, R. *Gas Production in Ullmann's Encyclopedia of Industrial Chemistry*, 5th ed.; VCH Publishers: Weinheim, Germany, 1989; Vol. A12.